Gulf Stream System Assimilation Experiments: A Sensitivity Study

PAOLA MALANOTTE-RIZZOLI AND ROBERTA E. YOUNG

Department of Earth, Atmospheric and Planetary Sciences, Massachusetts Institute of Technology, Cambridge, Massachusetts

(Manuscript received 9 May 1995, in final form 7 December 1995)

ABSTRACT

The major objective of oceanic data assimilation studies has been thus far to obtain a four-dimensional realization (space plus time) of the oceanic flow simultaneously consistent with the observations and the model dynamics. In these latest years, however, the forecasting of oceanic motions has emerged as a legitimate and important goal per se. In particular, the operational prediction of mesoscale flows and frontal systems has been the objective of recent assimilation applications in various regional systems of the World Ocean. One such effort focused on the short-term prediction of the Gulf Stream system in the DAMEE GSR (Data Assimilation and Model Evaluation Experiments Gulf Stream Region) sponsored by the U.S. Navy. The objective of DAMEE GSR phases I and II was 1–2-week forecast experiments. Phase III extended the suite of case studies by adding a 2-month-long assimilation experiment to assess the impact of long-term assimilations on model performance and forecasting skill.

In this paper the authors report the results of DAMEE GSR phase III but broaden the perspective by addressing two further issues, namely, the model sensitivity to the choice of the initial fields and the frequency of intermittent data assimilation. Two versions of the OTIS-3 (Optimum Thermal Interpolation System) of the U.S. Navy Fleet Numerical Oceanography Center were available, providing slightly different distributions of temperature and salinity over the entire Gulf Stream system. They are referred to as OTIS-3a, available with biweekly frequency from 4 May 1988 through 28 December 1988, in the context of a different assimilation work; and OTIS-3b, provided by the DAMEE GSR phase III effort, for the 2-month period 4 May–4 July 1988, with a slightly irregular frequency, weekly on the average. The main results can be summarized as follows.

The intermittent assimilation of the OTIS-3b datasets with average weekly frequency profoundly improves the model forecasting skill. Without assimilation the model never beats persistence. With the assimilation, the model-predicted Gulf Stream north wall is in excellent agreement with the verification infrared (IR) north wall, remaining always within the error bar of the IR north wall estimate, ± 15km.

Two types of sensitivity experiments to the initial conditions were carried out: first, reconstruction of the initial fields with the two different OTIS-3a and OTIS-3b datasets but with the same initialization method; second, reconstruction of the initial fields with the same OTIS-3a dataset but with two different initialization methods. The results show that the initial velocity field is much more crucial in affecting the model evolution and hence its predictive skill as it determines the stability properties of the Gulf Stream jet. Hence, it is very important to use the same dynamical initialization for velocity when starting from different distributions of temperature and salinity, as the jet profiles thus obtained will be very similar in structure and strength. This identical dynamical initialization will allow meaningful comparisons of experiments that start from slightly different density distributions.

Finally, we compare weekly assimilations of OTIS-3b with biweekly and monthly assimilations of OTIS-3a, initialized with the same procedure. The authors conclude that a weekly assimilation of the global OTIS-3 dataset is not necessary and that a biweekly assimilation is equally effective in improving the model predictive skill.

1. Introduction

Until recently the motivation for oceanic data assimilation has not been the prediction of the ocean circulation, while, on the other hand, the need of forecasting the weather spurred the growth of data assimilation in meteorology as early as two decades ago. Two major objectives can be identified as characterizing the majority of oceanic assimilation studies. The first one is to quantitatively use the data for model improvement, that is, to correct for the many deficiencies of ocean general circulation models (OGCMs) such as parameterizations of subgrid-scale processes, poorly known boundary conditions, etc. The second objective is to obtain a four-dimensional realization (the spatial description coupled with the time evolution) of the oceanic flow simultaneously consistent with the observations and the model dynamics.

In these latest years, however, the forecasting of oceanic motions has emerged as a legitimate and important

Corresponding author address: Dr. Paola Malanotte-Rizzoli, Dept. of Earth, Atmospheric and Planetary Sciences, Massachusetts Institute of Technology, Room 54-1416, Cambridge, MA 02139-4307.
E-mail: rizzoli@ocean.mit.edu

© 1997 American Meteorological Society

Unauthenticated | Downloaded 06/21/21 02:08 AM UTC

goal. Oceanic predictions are now needed in very diverse problems and on very different timescales, from 100 years in climate problems, through interannual climate variability and extended seasonal weather forecasting, to a few weeks in regional ocean forecasting. In this latter category, an important example is the interest of navies in ocean frontal systems, such as the prediction of the Gulf Stream front and of its meandering on a timescale of two to four weeks. The operational prediction of such synoptic motions has been the objective of recent assimilation applications in various regional systems of the World Ocean.

One such effort focused on the short-term prediction of the Gulf Stream system in the DAMEE GSR (Data Assimilation and Model Evaluation Experiments Gulf Stream Region) for which the strong motivation was provided by the U.S. Navy's persistent need for improved capability in ocean nowcast–forecast systems (Willems et al. 1994). The objective of DAMEE GSR was to assess quantitatively the nowcast–forecast capability of specific ocean models and the impact data assimilation has on these capabilities using the North Atlantic Gulf Stream region, roughly 20° in latitude by 30° in longitude, as a regional test basin.

DAMEE GSR was conducted in three phases. Phase I was designed to evaluate a model's forecast capability using common initial conditions and comparing 1 week model forecast fields with observations. Phase II added data assimilation to assess its impact on forecast capability, using the same case studies as in phase I (Willems et al. 1994). Phase III extended the suite of case studies by adding a 2-month-long case for assessment of model performance with extended assimilations.

The purpose of this study is to report on the results of DAMEE GSR phase III but with a broader perspective than short-term prediction only. A first issue addressed in this work is the sensitivity of the model's unconstrained evolution, that is, without data assimilation, to the choice of the initial field, which includes different observational datasets as well as different dynamical initialization procedures. A second issue addressed is the sensitivity of the model forecasting skill to the frequency of data assimilation. The current assimilations carried out are in fact intermittent in that the assimilated observations are provided with biweekly frequency over an extended (6 months) period and with weekly frequency only over the periods of the DAMEE GSR case studies. The problem of frequency of assimilation is obviously related to the intrinsic predictability timescale of the model, that is, the timescale over which the model loses the memory of the initial state.

The paper is organized as follows. Section 2 discusses the modeling components of the overall assimilation procedure, that is, the OGCM used and its configuration in the Gulf Stream system (section 2a); the assimilation method (section 2b); and the measure of performance used to assess the model forecast skill (section 2c). Section 3 describes the dataset available for assimilation and addresses the sensitivity of the model unconstrained evolution to different initial observational fields and/or initialization procedures. Section 4 presents the results of the different assimilation experiments. Specifically, section 4a gives the results of the 2-month-long assimilation experiment of DAMEE GSR phase III. Section 4b assesses the sensitivity of model performance to the frequency of intermittent data assimilations by comparing biweekly and monthly assimilations. Finally, in section 5 we summarize the conclusions and the main results of the current study.

2. Modeling components of the assimilation procedure

a. The ocean circulation model

The ocean circulation model is the Semi-spectral Primitive Equation Model (SPEM) that was originally developed by D. Haidvogel for coastal and regional process studies (Haidvogel et al. 1991). The model has been adapted by us to the Gulf Stream system in collaboration with D. Haidvogel, K. Hedström, and A. Beckmann.

The model integrates prognostically the primitive equations for an incompressible, hydrostatic, Boussinesq rotating fluid in the rigid-lid approximation. The model contains active thermodynamics having a prognostic advective–diffusive equation for the perturbation density field $\rho(x, y, z, t)$. The total density is given by

$$\rho^* = \rho_0 + \overline{\rho}(z) + \rho(x, y, z, t), \tag{1}$$

where ρ_o is a bulk density value and $\overline{\rho}(z)$ is the resting background density profile.

The equations of motion are modified by two coordinate transformations. The first is one in which the vertical Cartesian coordinate is replaced by the topography-following variable:

$$\sigma = 1 + 2\frac{z}{h}, \tag{2}$$

where $h(x, y)$ is the local depth of the fluid. The model configuration covers the entire Gulf Stream system, between 75° and 50°W in longitude and 29° and 46°N in latitude. The topography for the model domain is shown in Fig. 1a. The realistic topography is taken from the SYNBAPS-II dataset of NOAA, now part of the ETOP05 dataset available through NCAR. It is truncated to a minimum depth of 500 m, thus specifically excluding from the domain the northern shelf. It has been smoothed using a spatially dependent Shapiro algorithm (J. Wilkins 1992, personal communication) to minimize pressure gradient errors introduced by the σ coordinate (see the appendix for more details).

The second transformation is a horizontal transformation to coastal-following orthogonal curvilinear coordinates with variable horizontal resolution. The coastline used follows the 500-m bathymetry contour. The model has 129 grid points in the along-coast direction

Unauthenticated | Downloaded 06/21/21 02:08 AM UTC

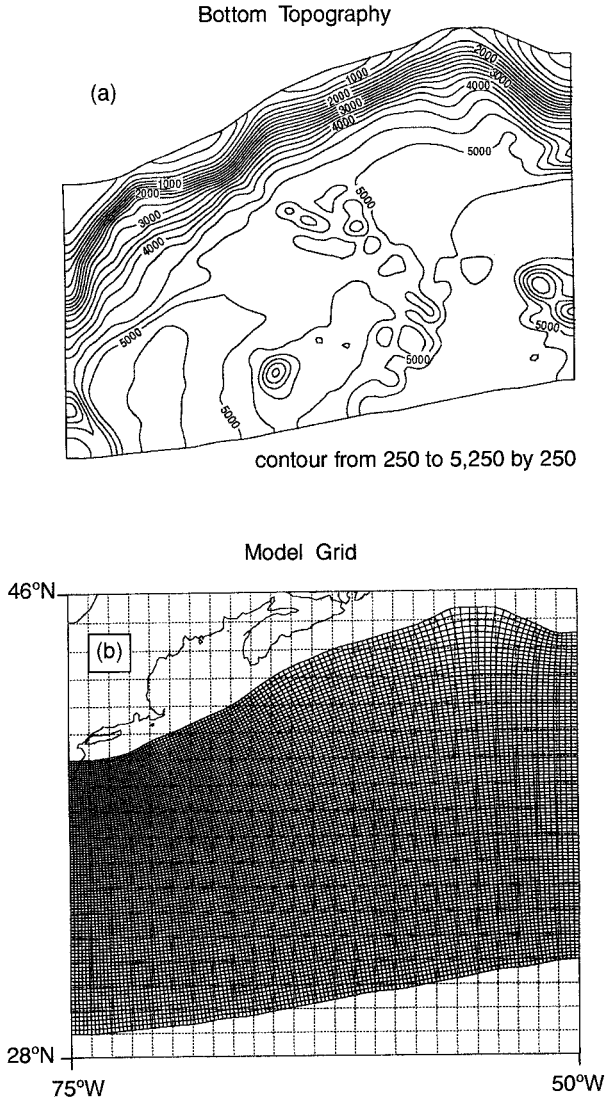

FIG. 1. Model domain from 50° to 75°W and 29° to 46°N. (a) Bottom topography. (b) Horizontal curvilinear coordinate grid.

and 97 grid points in the coastward direction, resulting in an average horizontal resolution of approximately 15 km. Thus, the model is fully eddy resolving in the Gulf Stream system. The curvilinear coordinate grid designed for the model domain is shown in Fig. 1b. The details of the equations of motion resulting from these two transformations are given in the appendix.

The upper surface of the model is a rigid lid at which momentum fluxes, density fluxes, and vertical velocity are set to zero. At the bottom surface the same boundary conditions apply. Thus, there is no wind or thermal forcing in the current simulations. The surface and bottom boundary conditions in σ coordinate are given in full detail in the appendix.

The horizontal boundary conditions at the four lateral boundaries of the domain have been specifically designed for the Gulf Stream system simulations. Boundary conditions must be prescribed for the prognostic variables (u, v, ρ) as well as for the transport streamfunction on the lateral edges (see the appendix). The northern edge of the domain, given by the 500-m isobath, represents the coast, as we do not extend the calculations over the shelf region. This edge is taken to be a region of no flow and zero transport is assigned to it. The other three boundaries are ''open'' boundaries. The eastern and western inflow–outflow conditions and the southern boundary condition are prescribed by the OTIS-3 dataset (Optimum Thermal Interpolation System) discussed in the following section. The initial conditions are also obtained from the global OTIS-3 datasets and will also be discussed in the next section.

The vertical (σ) dependence of the model prognostic variables is given as an expansion in specially constructed numerical polynomials $P_n(\sigma)$, according to

$$f(\xi, \eta, \sigma, t) = \sum_{n=0}^{N} a_n(\xi, \eta, t)P_n(\sigma), \qquad (3)$$

where f represents any model variable (u, v, ρ) and $a_n(\xi, \eta, t)$ is the amplitude of the nth mode. Thirteen modified polynomials are used in the current simulations where the $n = 0$ polynomial represents the barotropic mode. The construction of the polynomials $P_n(\sigma)$ is described in the appendix. The use of the specially constructed polynomials as the vertical expansion basis ensures an increased vertical resolution in the sharp permanent pycnocline of the Gulf Stream in order to adequately resolve the internal dynamics and baroclinic instabilities of the Gulf Stream jet and associated eddy field. The polynomial dependence on the vertical coordinate is based upon a prescribed mean density profile $\bar{\rho}(z)$ representative of the climatological condition for this region evaluated as exponential fit to the OTIS-3 data. The actual algorithm for constructing the numerical polynomials and supporting matrices for the model spectral calculation was provided by D. Haidvogel. Table 1 summarizes the values of the parameters used in the numerical experiments.

b. The assimilation method

There are three basic changes in the model configuration used in the current work with respect to the one used in other assimilation studies (Malanotte-Rizzoli and Young 1995). The first change concerns the choice of boundary values for the prognostic variables (u, v, ρ) and the transport streamfunction (Ψ) at the four lateral edges of the model domain. The assimilation version of the SPEM model updates the edge boundary values at every time step using field values that are linearly interpolated in time between two successive observational datasets (u, v, ρ, and Ψ on the SPEM model grid). For the nonassimilation version of the code, the edge values remain fixed to the initialization fields.

The second change is the addition of a three-edge

Unauthenticated | Downloaded 06/21/21 02:08 AM UTC

TABLE 1. Parameter values used in assimilation experiments.

Symbol	Value	Definition
L	129	Number of points in ξ direction
M	97	Number of points in η direction
N	12	Number of baroclinic modified polynomials
ρ_0	1027.67 kg m^{-3}	Constant reference density
$\overline{\rho}$(z)	$1027.9-1.7\exp(-z/750.0)-\rho_0$	Background density stratification
g	9.80 m s^{-1}	Acceleration of gravity
T	2 days	Nudging timescale
ν	1×10^{11} m^4 s^{-1}	Biharmonic diffusion coefficient
κ	0.0	Vertical difussion coefficient
$h_{\min}$	250 m	Minimum water depth
$h_{\max}$	5250 m	Maximum water depth
Δt	12 min (720 s) 120 steps day^{-1}	Time step
f	from 7.2×10^{-5} to 1.04×10^{-4}	Coriolis parameter

sponge to the inflow, outflow, and coastal regions of the model. This sponge region is shown in Fig. 2a. The field evolution equations for the prognostic variables have linear Newtonian relaxation terms added to the model forcing. If F represents one of the prognostic variables (u, v, ρ), then the change may be written as

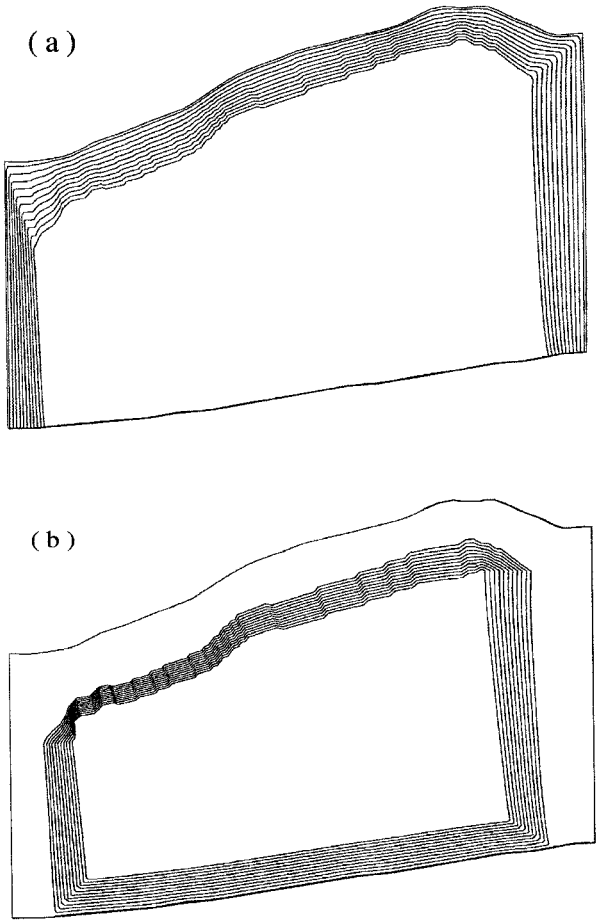

FIG. 2. Regions of enhanced model forcing for assimilation version of SPEM. (a) Three-edge sponge for boundaries. (b) Interior time-dependent nudging region.

$$\frac{\partial F}{\partial t} = \text{RHS} - R_{\text{sponge}}(F - F_{\text{reference}}), \tag{4}$$

where RHS contains all the remaining terms of the dynamical equation for the variable F. For this sponge region, the maximum value of R_{sponge} is (2 days)$^{-1}$ at the eastern, northern, and western edges of the model domain; $R_{\text{sponge}}(\xi, \eta)$ decreases linearly to zero on the interior of the model domain. The shaded portion of Fig. 2a shows the extent of the nonzero region for this sponge. The field $F_{\text{reference}}$ in the nonassimilation version of the code is the initial field, while in the assimilation version of the code it contains values that are updated at every model time step. The eastern and western regions of this sponge allow for the direct assimilation of the time evolution of the axis of the Gulf Stream as it enters and exits the model domain. Information about the entrance–exit angles of the jet axis would not be provided to the model if the boundary conditions were specified only at the domain edges. Also, use of the sponge layers in open outflow regions has been shown empirically to provide reasonable outflow boundary conditions (Chapman 1985). The coastal portion of this sponge is important since the domain for the SPEM model is not configured to handle the small-scale coastal processes. The coastal sponge helps to damp spurious small-scale features that would tend to appear in this shallow region without it.

The third change is the addition of an internal nudging region in the model for the interior assimilation of the observationally derived three-dimensional (u, v, ρ) datasets. The prognostic equations have an additional Newtonian nudging term added to the forcing on the velocity and density variables. For F representing one of the variables (u, v, ρ), this third change may be written as

$$\frac{\partial F}{\partial t} = \text{RHS2} - R_{\text{nudge}}(F - F_{\text{data}}), \tag{5}$$

where RHS2 contains not only the remaining terms of the dynamical equation but also the edge sponge described above. The factor $R_{\text{nudge}}(\xi, \eta, t)$ is now both space

Unauthenticated | Downloaded 06/21/21 02:08 AM UTC

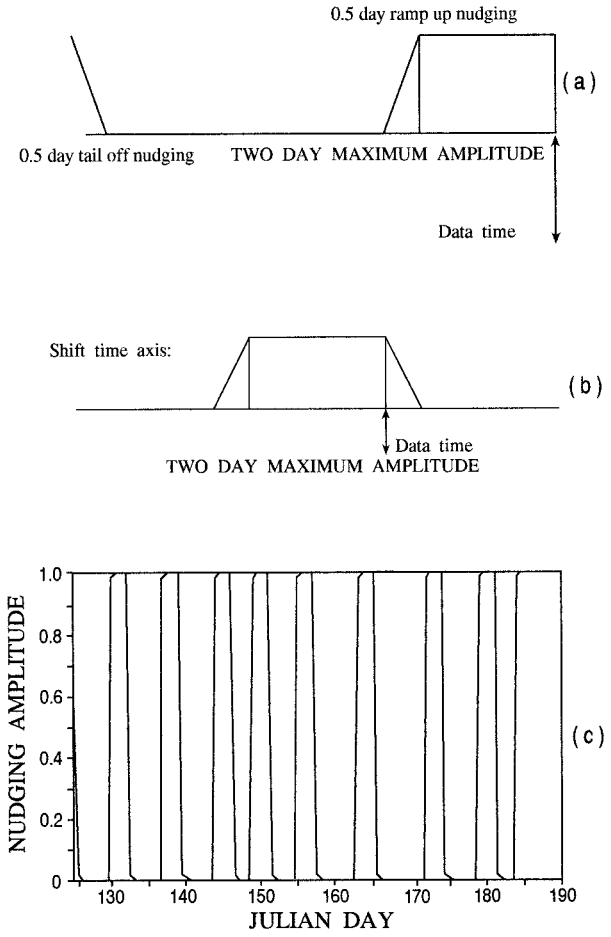

FIG. 3. Detailed description of the time dependence of the nudging amplitude. (a) Nudging amplitude for a given dataset from one Julian data day to the next Julian data day. (b) The total time a particular dataset is used for nudging. (c) Amplitude of maximum time-dependent nudging coefficient, OTIS-3b data variably spaced in time as listed in Table 2.

and time dependent. Figure 2b shows the spatial extent of the internal forcing for the data assimilation in the model. The maximum value of the sponge is in the central portion of the domain. The sponge amplitude (i.e., R_{nudge}) drops linearly to zero in the shaded boundary region of Fig. 2b. At the time of maximum forcing, R_{nudge} has the value of $(2 \text{ days})^{-1}$ in the central region. This maximum value determines how strongly the dynamical evolution of the model is relaxed toward the observation fields, that is, how much freedom is allowed the model to develop its internal dynamics (Malanotte-Rizzoli and Young 1995).

A time-intermittent assimilation is carried out to allow the model to evolve only according to its own internal dynamics during intervals when observations are unavailable. We carry out hindcast experiments; thus the data begin influencing the model evolution before the actual Julian day when they would become available. This is done to counter the phase shift in the model response introduced by the nudging factor in the model forcing (Malanotte-Rizzoli and Young 1995).

TABLE 2. Dates of available OTIS-3b data for DAMEE GSR Phase III. For the 2-month assimilation experiment, the assimilation algorithm was changed to use the available OTIS-3 data at the proper Julian date.

Date in 1988	Julian day
4 May	125
11 May	132
18 May	139
25 May	146
30 May	151
5 June	157
13 June	165
22 June	174
29 June	181
4 July	186

Figure 3 shows the time evolution of the assimilation nudging term R_{nudge} at a fixed point in the interior of the domain. Figure 3a shows the time dependence of the amplitude of R_{nudge} between consecutive observation days. For the first half day, when the amplitude is decreasing, the F_{data} would be the appropriate field (u, v, ρ) constructed from the earlier dataset. For the last 2.5 days (when the amplitude is increasing or holding constant), F_{data} would be from the sucessive dataset. Figure 3b shows the piecewise linear time duration of the assimilation term in the model for any particular dataset available at the assimilation day. The 2-month-long assimilation experiment of section 4a uses the actual Julian days of the observational datasets that were available at irregular time intervals. The dates of available OTIS-3 fields for this experiment are given in Table 2, and Fig. 3c shows the variably spaced peaks in the nudging amplitude for this experiment. The peak precedes each data time by 2 days. Figure 3c is a plot of the scaled nudging amplitude. For a given point in the interior, the nudging amplitude is scaled so that the time maximum has value of 1. The choice of this temporal weighting is discussed and justified in Malanotte-Rizzoli and Young (1995).

c. Measure of predictive skill

The measure of predictive skill is the one consistently used throughout the DAMEE GSR effort (Lai and Qian 1993) and is based upon comparing the Gulf Stream north wall as simulated by the model with independent infrared (IR) imagery from which the surface signature of the north wall has been extracted. The ''classical'' definition of the north wall is the intersection of the 15°C isotherm with the 200-m isobath (Halkin and Rossby 1985). From the Hall and Fofonoff (1993) Gulf Stream sections, the north wall is observed to have a salinity of 35.95 psu (G. Flierl, JGOFS data management program, 1994, personal communication). The North Wall density is then $\rho = 1026.7 \text{ kg m}^{-3}$. In the following, we show the horizontal density field at 200-m depth in which we actually plot

Unauthenticated | Downloaded 06/21/21 02:08 AM UTC

$$\rho_1 = \rho - \rho_{\text{northwall}} = \rho - 1026.7. \quad (6)$$

Thus, in the figures that follow, the north wall is visualized as the zero contour. S. Glenn has analyzed IR imagery for the entire period starting 4 May and running through December 1988 and has provided us with the digitized shapes of the surface north wall. Error bars on this frontal analysis were established based on the rule that stream location data available on the day of the analysis had an error of ± 15 km (Glenn et al. 1991). Cornillon and Watts (1987) systematically compared the surface signature of the Gulf Stream from 155 IR maps with the actual location of the 15°C isotherm at 200 m determined from inverted echo sounder measurements. They found that the Gulf Stream surface northern edge is consistently located approximately 14 km shoreward of the north wall. Consequently, we measure in the model the location of the north wall at 200 m and then shift it shoreward by 14 km perpendicular to itself to obtain its surface signature. We then measure the absolute area between the model surface north wall and the IR verification north wall and evaluate the average of the arc length of the two axes over the model domain. The mean offset of the model north wall is used as the measure of error:

$$\text{Error} = \text{mean GS offset} = \frac{\text{area between axes}}{\text{mean arc length of axes}}. \quad (7)$$

The mean offset errors in the model-predicted north wall in different assimilations, or even in the model unconstrained evolution, can then be compared against each other and assessed against persistence, defined as the prediction in which the initial condition is kept ''frozen.''

3. Model sensitivity to the initial conditions

In this section we first describe the dataset used for assimilation and then carry out numerical experiments to assess the model sensitivity to different initial observational fields and/or initialization procedures.

a. The datasets

The global dataset is provided by OTIS-3 developed by Cummings and Ignaszewski (1991) at the U.S. Navy Fleet Numerical Oceanography Center (FNOC) as part of a global data assimilation scheme. The subset covering the Gulf Stream system domain shown in Figs. 1a, b has been provided to us through the DAMEE GSR program. For parallel work carried out in the context of the SYNOP (Synoptic Ocean Prediction) program of the U.S. Navy, we obtained biweekly fields starting on 4 May 1988 and running through 28 December 1988. To establish a reference terminology we call this package OTIS-3a.

The OTIS-3 package provided by the DAMEE GSR phase III is slightly different, as described below. We call this package OTIS-3b, and the dates of available data provided to carry out the 2-month-long assimilation experiment of phase III are given in Table 2.

Both OTIS-3a and OTIS-3b provide three-dimensional distributions of temperature and salinity on a regularly gridded domain. Specifically, the vertical coordinate is a stretched grid consisting of 34 standard depth levels from the surface to 5000 m. The upper 1000 m are sampled more finely with 23 levels to resolve the mixed layer and the main thermocline. The horizontal grid has a resolution of 0.2° (~22 km) both in longitude and latitude. Both OTIS-3 packages provide optimally interpolated (OI) fields constructed by using the real-time database available at FNOC that comprises surface observations from ships, fixed and drifting buoys, satellite IR sea surface temperatures, and the U.S. Navy's Generalized Digital Environment Model (GDEM) climatology used as a first guess for the OI scheme. Feature models are used for the Gulf Stream jet and for warm and cold core rings whose surface positions are detected by IR imagery. For full details about the OTIS-3 package, see Cummings and Ignaszewski (1991).

The OTIS-3a package also provides at each mesh point the surface dynamic height evaluated with respect to 5000 m. As bottom velocities are assumed to be consistently very small, this surface dynamic height is given to the user as a good proxy for the actual sea surface height. This assumption may actually be a rather good one as proved by the very small velocities (maximum 2 cm s^{-1}) at 3000 m found in the region around 73°W (Halkin and Rossby 1985) and the very small velocities at approximately 4000 m measured at the eastern array throughout the SYNOP moorings deployment period (Malanotte-Rizzoli and Young 1995). The OTIS-3b package provided for the DAMEE GSR phase III on the other hand does not contain a sea surface height field. Thus, the two packages are slightly different.

For both versions of OTIS-3, temperature and salinity fields are converted to density using the standard nonlinear United Nations Educational, Scientific and Cultural Organization (UNESCO) equation of state (UNESCO 1981). A systematic check is then made to determine whether the water column is in hydrostatic balance. If hydrostatic instabilities are found, the column is vertically mixed until it is hydrostatically stable following the scheme introduced by Semtner (1974). As the OTIS-3 algorithms were specifically developed for deep water, many hydrostatically unstable regions are found in both OTIS-3 packages north of the 1000-m isobath. Given the frequency of vertical mixing necessary in the coastal shelf region, the density field is horizontally averaged over the continental slope region at each z level (fluid north of the 1000-m isobath). This maintains the vertical stratification characteristic of the slope water while removing spurious flows in this coastal region. The density at each of the 34 vertical levels is then bilinearly interpolated onto the SPEM horizontal

Unauthenticated | Downloaded 06/21/21 02:08 AM UTC

grid. The density field is smoothed with a Shapiro filter (order 2) to remove gridding noise. Two different initialization procedures can then be used to construct the geostrophically, hydrostatically balanced initial fields required by primitive equation models. The first procedure is the one used by Malanotte-Rizzoli and Young (1995) with the OTIS-3a package. We summarize it below.

The surface pressure is obtained from the sea surface height according to

$$p_0 = g\rho_0\zeta. \tag{8}$$

The hydrostatic relationship in the OTIS Cartesian vertical coordinate z,

$$\frac{\partial p}{\partial z} = -g\rho, \tag{9}$$

is then integrated downward at every horizontal grid point of the SPEM curvilinear grid starting from the surface value p_0 given by Eq. (8). Thus, the total pressure field is obtained. The horizontal velocity components are then evaluated from the geostrophic relationships:

$$u = -\frac{1}{\rho_0 f}\frac{\partial p}{\partial \eta}$$

and

$$v = \frac{1}{\rho_0 f}\frac{\partial p}{\partial \xi}. \tag{10}$$

Finally, the geostrophic velocities (u, v) and the density ρ are evaluated at the model vertical collocation points by linear interpolation in z.

The model transport streamfunction is found by setting its value to zero at the northern boundary of the domain and at each ξ point integrating along each coastward η line to provide

$$\psi(\xi, \eta) = \int_{\eta}^{0}\int_{-1}^{+1}\frac{h}{2}u\, d\eta\, d\sigma. \tag{11}$$

The northern edge follows the 500-m isobath and represents the border of the continental shelf. The boundary condition of zero total transport is used because of the well-known evidence that there is very little total mass exchange between the shelf and the deep ocean, as the continental slope acts as an insulator (Chapman and Brink 1987).

The OTIS-3b package provided for the DAMEE GSR phase III lacks a sea surface height field. Thus, a ''level-of-no-motion'' calculation is performed to compute the geostrophic flow fields consistent with the density fields derived from the OTIS-3b data. An assumption is made that there is no flow at depths below 2000 m; that is, the density field values below 2000 m are replaced with the horizontally averaged value at 2000 m. A reference pressure value P_{2000} is chosen by integrating the weight of the fluid above 2000 m and horizontally averaging this value. The pressure for the fluid above 2000 m is then found by integrating hydrostatically upward from the following reference value:

$$P(\xi, \eta, z) = P_{2000} - \int_{z}^{2000\ \mathrm{m}} g\rho(\xi, \eta, z)\, dz. \tag{12}$$

From these pressures, the geostrophic velocities on the model grid at the OTIS levels above 2000 m can be calculated:

$$u(\xi, \eta, z) = -\frac{1}{\rho_0 f}\frac{\partial P}{\partial \eta} \tag{13a}$$

$$v(\xi,\eta, z) = +\frac{1}{\rho_0 f}\frac{\partial P}{\partial \xi}. \tag{13b}$$

Linear interpolation between the velocity and density values on the OTIS depths is performed to generate the velocity and density values at the model vertical collocation points. The transport streamfunction is then evaluated according to Eq. (11). Both initialization procedures can be used with OTIS-3a, while only the second one can be applied to OTIS-3b.

b. Sensitivity to different initial fields

Different initial conditions may enhance or reduce a model's predictive skill, so the model's sensitivity to initial conditions must be assessed. This is especially true in the current case as two OTIS-3 packages are available that differ in the three-dimensional structure of the temperature and salinity fields, and they provide slightly different realizations even when treated with the same balanced initialization procedure. In this section we assess SPEM sensitivity to the initial fields by carrying out two types of experiments: (i) initialization with the two different OTIS-3a and OTIS-3b fields treated with the same initialization, the level-of-no motion procedure of section 3a; (ii) initialization with the same OTIS-3a fields treated with the two different initializations of the previous section. In these experiments no assimilation is carried out, thus the model evolves unconstrained from the prescribed initial condition. A model-to-model comparison is then carried out by measuring the mean offset of the two experiments north walls as defined by Eq. (7). The growth of this model-to-model mean offset is assessed against persistence of the initial condition, where the true IR north walls are used in the persistence test.

We show first the difference in the initial fields when using the two OTIS-3 datasets initialized with the same level-of-no-motion procedure, the only one feasible for OTIS-3b. Figure 4 shows the density field at 200 m, where the zero contour marks the position of the north wall according to Eq. (6), for 4 May 1988. The top panel shows the density field reconstructed from OTIS-3a; the bottom panel, the one reconstructed from OTIS-3b. The difference between the two fields is quite ev-

Unauthenticated | Downloaded 06/21/21 02:08 AM UTC

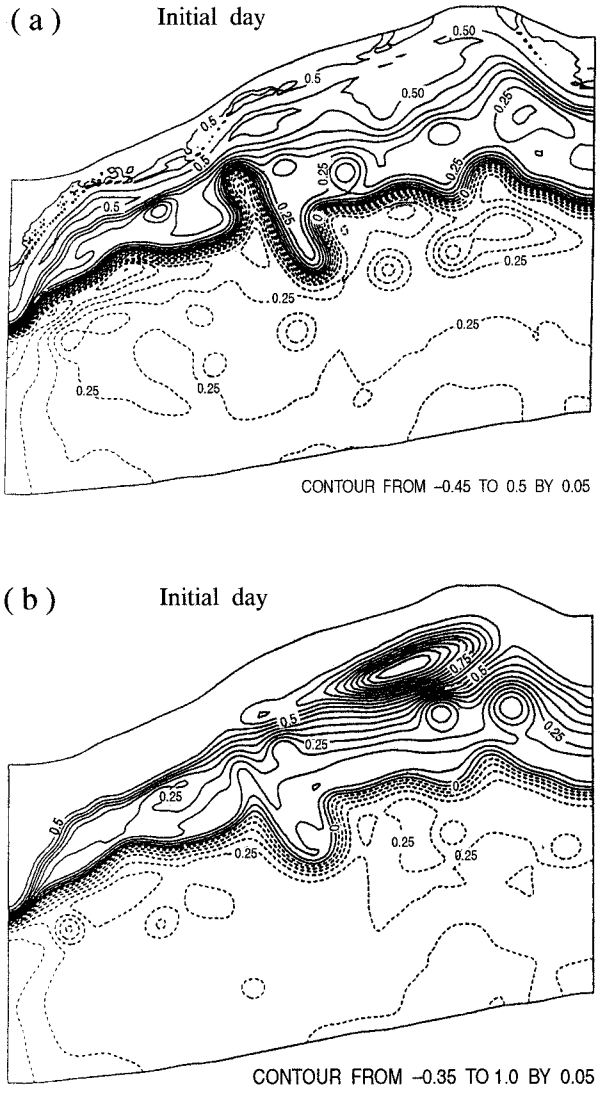

FIG. 4. Model initial conditions using level of no motion at 2000 m for 4 May 1988. (a) OTIS-3a density at 200 m with zero contour set to the classical north wall. (b) OTIS-3b density at 200 m with zero contour set to the classical north wall.

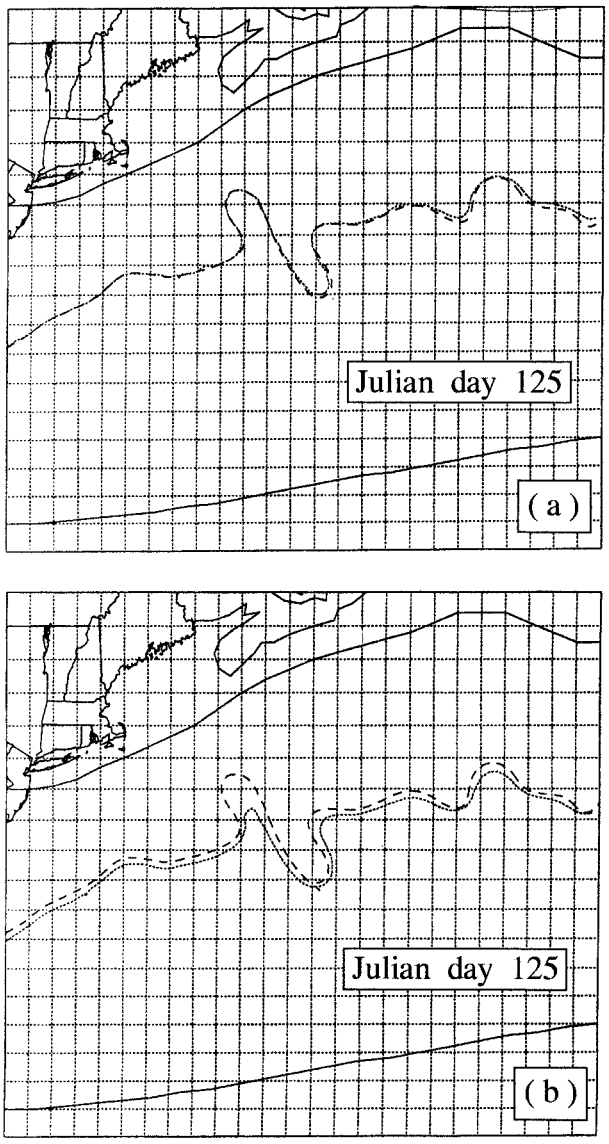

FIG. 5. OTIS-3 initial conditions for 4 May 1988. (a) OTIS-3a: finely dashed line is the classical north wall shifted shoreward by 14 km. Compare to the IR north wall location given by the widely dashed line. (b) OTIS-3b: finely dashed line is the classical north wall shifted shoreward by 14 km. Compare to the IR north wall location given by the widely dashed line.

ident, with the Gulf Stream interior meander much more steepened (in the top panel) surrounding a warm core center that is not present in the bottom panel. Also, the difference in the slope and Sargasso Sea interior fields suggests that possible differences in the feature models may exist in the two packages. Notice, for instance, the intense recirculation over the northern continental slope present in the OTIS-3b field (bottom panel of Fig. 4), which is completely absent in the OTIS-3a field.

A second important difference is found when comparing the two OTIS-3 north wall with the north wall IR imagery positions. Figure 5 shows the 4 May 1988 OTIS-3a north wall (thinly dashed line) versus the IR one (broadly dashed line) in the top panel, and the same comparison for the OTIS-3b north wall (bottom panel). The OTIS-3a north wall agrees extremely well with the IR one. The OTIS-3b north wall, on the other hand, has a systematic southward shift over the entire Gulf Stream jet. The behavior shown in Fig. 5 is consistently found in all the days in which the OTIS-3 distributions are available. In particular, the systematic southward shift of the OTIS-3b north wall is present in all the days of the DAMEE GSR 2-month experiment; the days are given in Table 2. We measured this southward shift from the IR north wall for all the days of Table 2 and evaluated for it an average value of 21 km, which is slightly greater than the error bar of ± 15 km of the IR north

Unauthenticated | Downloaded 06/21/21 02:08 AM UTC

wall estimate. We have to correct for this systematic error in order to carry out meaningful comparisons with the IR north wall when assimilating the OTIS-3b fields. Thus, in these latter assimilations, we consistently shift southward by 21 km the IR north wall for all the days of Table 2 before evaluating the model north wall mean offset according to Eq. (7). No shift of the IR north wall is performed when assimilating the OTIS-3a fields.

In the first experiment we tested the model sensitivity to different distributions of temperature and salinity and, hence density, by using the same level-of-no-motion procedure to obtain initial fields from both the OTIS-3a and OTIS-3b datasets. The corresponding initial density fields for 4 May 1988 are those shown in Fig. 4. We then carried out two unconstrained prognostic calculations from these two initial conditions and perform a model-to-model comparison by measuring the mean offset between the model north walls of the two calculations.

Figure 6a shows such mean offset (solid line) against persistence of the initial IR north wall (dashed line). A mean offset of approximately 15 km is present in the initial fields due to the difference between the two OTIS-3 datasets. As the OTIS-3a 4 May 1988 north wall agrees quite well with the IR one (Fig. 5, top panel), this initial mean offset is basically the one existing between the OTIS-3b north wall and the IR one (Fig. 5, bottom panel). The mean offset remains approximately constant at an average value of 20 km for the first 40 days of the evolution, increasing exponentially only thereafter. Thus, the two different initial conditions due to the temperature–salinity differences in the two OTIS-3 datasets do not alter substantially the evolution of the Gulf Stream jet for a period of approximately 40 days.

The second test is carried out by initializing the model with the same OTIS-3a package but using the two different initializations discussed in the previous section. In the first of these initializations the reconstructed velocity field is nonzero down to the bottom. Again, we carried out two unconstrained prognostic calculations starting from the two different initial fields and measured the mean offset of the model north walls in the two experiments. Figure 6b shows such model-to-model mean offset (solid line) versus persistence of the initial IR north wall (dashed line). The behavior of the mean offset in Fig. 6b is rather worse than the one in Fig. 6a, as it grows exponentially beyond 20 km only after 20 days, indicating a much more rapid divergence in the behavior of the Gulf Stream jet in these two calculations.

These two tests of model sensitivity to the initial condition indicate that the initial velocity field is much more crucial than the initial density field in affecting the model evolution and hence its predictive skill. The initial velocity field determines, in fact, the stability properties of the Gulf Stream jet and hence its consequent dynamical behavior. For the experiments initialized with different OTIS-3 datasets but an identical initialization procedure the initial density distributions are different, as evident from Fig. 4. However, the velocity fields reconstructed with the level-of-no-motion method are very similar in quantities such as total across-channel transport and Gulf Stream jet velocity structure and strength. The initial across-channel transports for these two experiments (not shown) are both on average approximately 40 Sv, thus rather unrealistic, and have a very similar behavior, decreasing from the western to the eastern boundary of the channel. The across-channel transport of OTIS-3a reconstructed assuming a sea surface height is on average twice as strong, approximately 80 Sv, thus much more realistic, and increases from the western to the eastern boundary of the channel. We point out that the realism of the initial fields, and of the subsequent behavior of the Gulf Stream jet, is not the objective of these experiments, which are aimed to assess

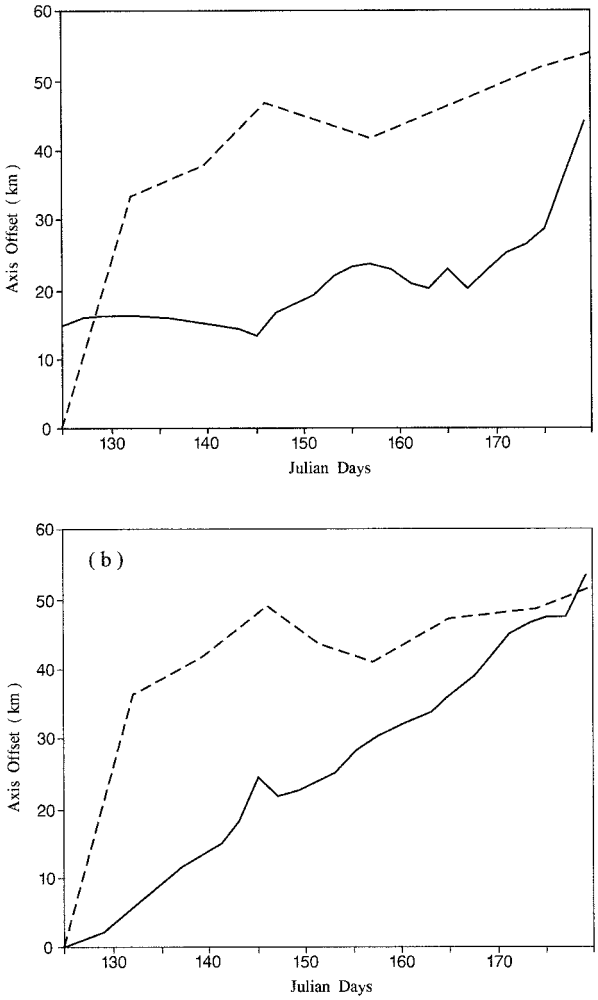

FIG. 6. Evolution of the model classical north wall in time. (a) Compare level-of-no-motion initialization for OTIS-3a to level-of-no-motion initialization for OTIS-3b (solid line). Dashed line: persistence test. (b) Compare level-of-no-motion initialization for OTIS-3a to initialization using the OTIS-3a dynamic height (solid line). Dashed line: persistence test.

Unauthenticated | Downloaded 06/21/21 02:08 AM UTC

the model sensitivity to the initial conditions, no matter how ''good'' or ''bad'' they are.

Also, the jet along-channel velocity structures reconstructed with the two initializations differ substantially. Figures 7a–c show the downstream u velocity component of the Gulf Stream jet in a meridional cross section at approximately 68°W. Specifically, Fig. 7a shows the downstream velocity core obtained from OTIS-3a with the level of no motion at 2000 m; Fig. 7b shows the same velocity core obtained with the level of no motion at 2000 m but from OTIS-3b. The two jets are almost identical both in structure and in maximum strength. As evident, the fluid is initially motionless below 2000 m. On the other hand, using the sea surface height of OTIS-3a to reconstruct the velocity structure, we obtain the jet of Fig. 7c. This is obviously very different from Figs. 7a,b as it reaches the bottom. Dynamically different initial jets will provide rapidly diverging evolutions. It is therefore very important to consistently use the same dynamical initialization method when dealing with slightly different temperature–salinity packages in order to compare meaningfully experiments with different initial fields.

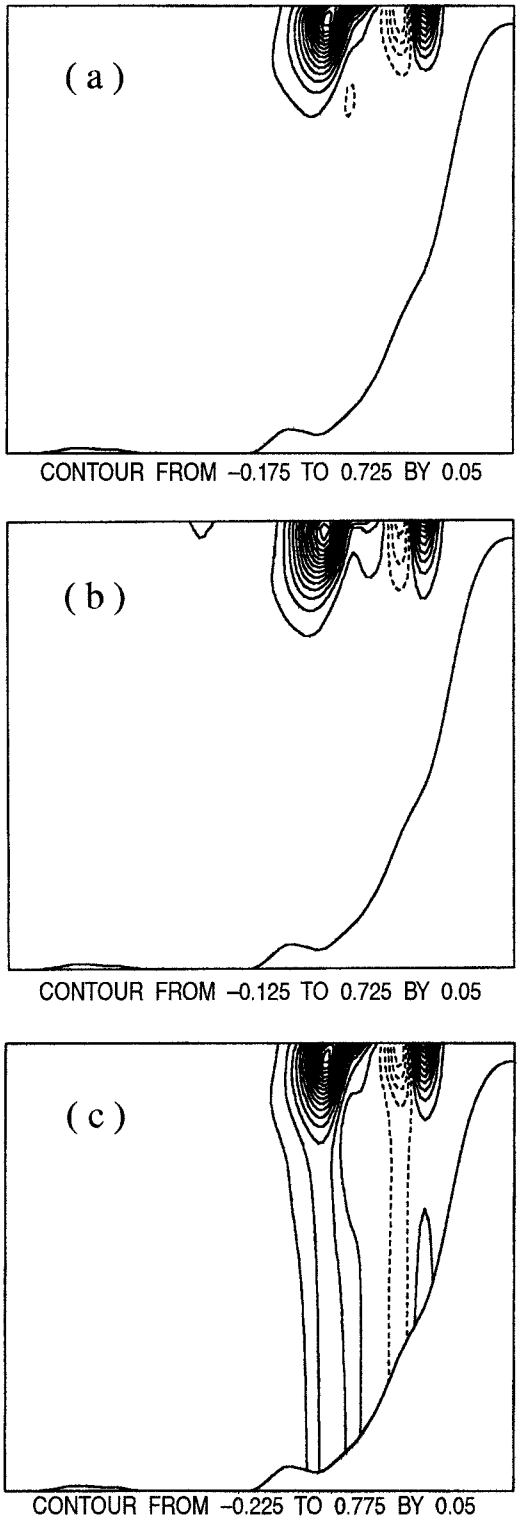

FIG. 7. Upstream eastward velocity cross section at ~68°W. (a) Level-of-no-motion initialization for OTIS-3a. (b) Level-of-no-motion initialization for OTIS-3b. (c) OTIS-3a initialization using the OTIS-3a dynamic height.

4. Assimilation experiments

In this section we present the results of the assimilation experiments carried out with the two different datasets OTIS-3a and OTIS-3b and with different frequencies of intermittent assimilations. To compare such experiments with different initial density distributions, we use the same initialization procedure of the level of no motion at 2000 m for all of them, as discussed in the previous section.

a. DAMEE GSR phase III assimilation experiment

For this 2-month-long experiment OTIS-3b datasets were provided at the dates given in Table 2, irregularly spaced in time. Thus, the assimilation frequency was also variable in time, even though it was of 1 week on the average.

Figure 8a shows the Gulf Stream north wall mean offset from the IR imagery north wall available on the days listed in Table 2 in the unconstrained model evolution, that is, with no OTIS-3b assimilation, starting from the OTIS-3b initial field for 4 May 1988 (solid line) assessed versus persistence (dashed line). The model never beats persistence in a statistically significant way. On the other hand, when assimilating the OTIS-3b datasets with an average weekly frequency (Fig. 8b), the model skill is excellent. The north wall mean offset in the assimilation (solid line in Fig. 8b) not only beats persistence significantly but is also within the error bar of the IR north wall estimate, ± 15 km.

Figures 9 and 10 are shown to illustrate the best and worst comparison between this 2-month-long OTIS-3b assimilation and the IR imagery verification dataset.

Unauthenticated | Downloaded 06/21/21 02:08 AM UTC

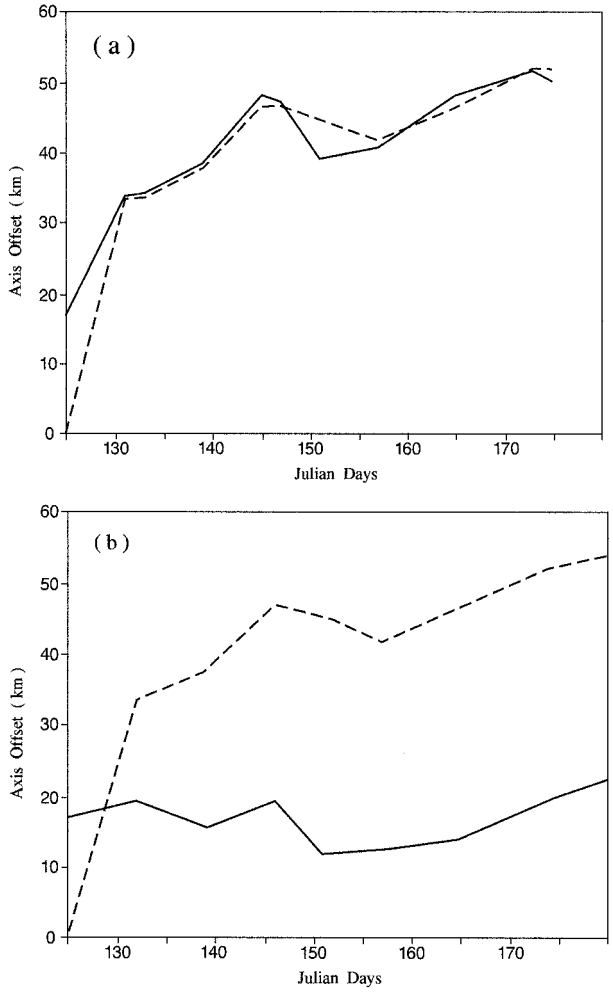

FIG. 8. Two-month prediction results. Model starting 4 May 1988. (a) No assimilation: solid line for the model, dashed line for persistence. (b) Time-varying OTIS-3b assimilation: solid line for the model, dashed line for persistence.

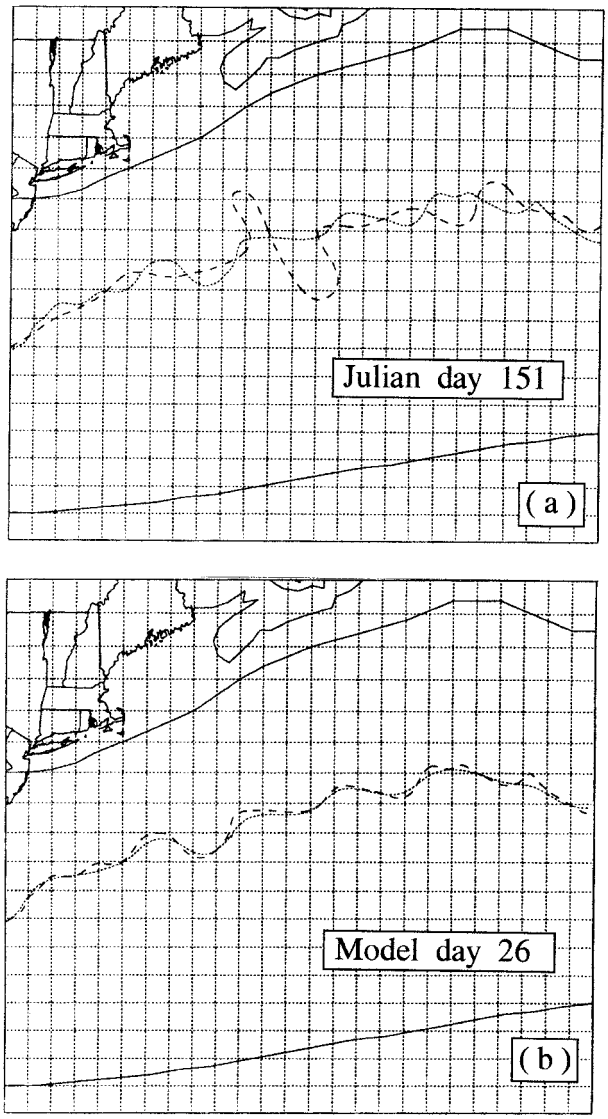

FIG. 9. Two-month prediction results. Model starting 4 May 1988. (a) Persistence compared to OTIS-3b north wall on 30 May 1988: Widely dashed line is persistence of 4 May 1988 front. Finely dashed line is IR north wall on 30 May 1988. (b) Assimilation best case: Julian day 151 (30 May 1988): Widely dashed line is IR north wall on 30 May 1988. Finely dashed line is model predicted front.

Figure 9 gives the best day, Julian day 151 (30 May 1988), which is 26 days into the calculation. Specifically, Fig. 9a shows the comparison between persistence, the north wall of 4 May 1988 (widely dashed line), and the north wall of 30 May 1988 (finely dashed line). Figure 9b shows the assimilation results by comparing the 30 May true north wall (widely dashed line) with the model-predicted front for the same day. The mean model offset is of 10 km for this day.

Figure 10 gives the worst day, Julian day 186 (4 July 1988), 61 days into the assimilation experiment. Again, Fig. 10a compares persistence, the north wall of 4 May (widely dashed line) with the north wall of 4 July (finely dashed line). Figure 10b gives the true north wall of 4 July, (widely dashed line) versus the model-predicted front for the same day (finely dashed line). Even in this worst case, the model mean offset is only approximately 23 km (final point in solid line of Fig. 8b).

Notice that not only the best case, Julian day 151 (Fig. 9), is a day of assimilation but also the worst case, Julian day 186 (Fig. 10), is a day of assimilation. In these experiments we clearly assimilate the Gulf Stream north wall provided by OTIS-3b package. However, the assimilated north wall is different from the verification north wall, the one estimated from IR imagery by S. Glenn. This is proved by Fig. 10, in which the assimilated north wall at the assimilation day 186 is rather different from the verification IR north wall, even though ''some'' IR-estimated north wall goes into OTIS-3b. Thus, we can assess that the SPEM model has excellent skill in hindcasting mode for tracking the Gulf

Unauthenticated | Downloaded 06/21/21 02:08 AM UTC

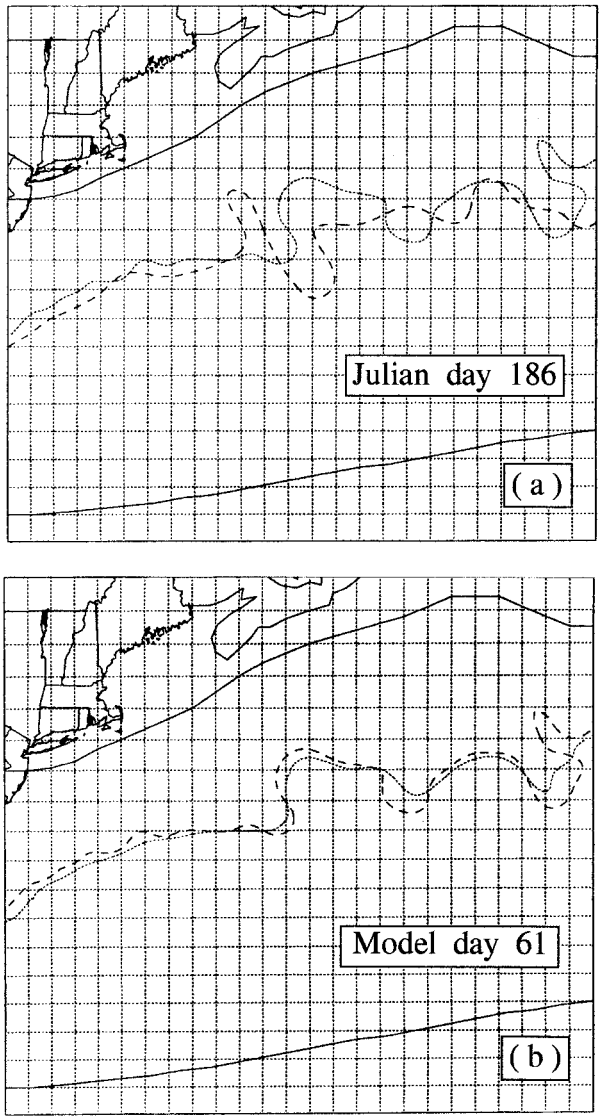

FIG. 10. Two-month prediction results. Model starting 4 May 1988. (a) Persistence compared to OTIS-3b north wall on 4 July 1988: Widely dashed line is persistence of 4 May 1988 front. Finely dashed line is IR north wall on 4 July 1988. (b) Assimilation worst case: Julian day 186 (4 July 1988): Widely dashed line is IR north wall on 4 July 1988. Finely dashed line is model predicted front.

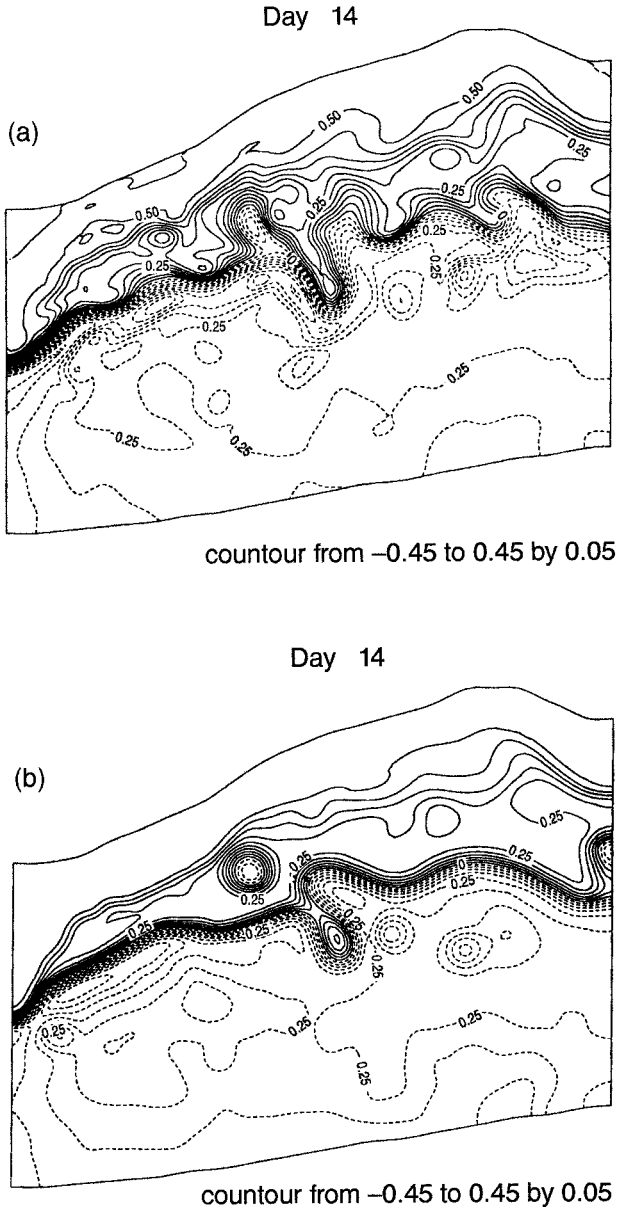

FIG. 11. (a) Density anomaly field at 200 m in the model unconstrained evolution after 14 days starting from the initial condition for 4 May 1988, upper panel of Fig. 4. (b) Corresponding density anomaly field from OTIS-3a at day 14, real time 18 May 1988.

Stream front when assimilating OTIS-3b on an average weekly frequency.

We also want to assess the predictive skill of SPEM in unconstrained evolution, that is, in forecasting mode under different initializations. First, we show the evolution from the initial condition of 4 May 1988, obtained with the OTIS-3a package, a level-of-no-motion initialization, which is shown in the upper panel of Fig. 4. The only forcing in this experiment is provided by the boundary conditions that obey persistence, that is, are kept identical to the initial conditions, as the only known values at the start. We ran this experiment for a total of 100 days, which allowed us to note that the initially smooth Gulf Stream jet had evolved into a very convoluted jet, one very different from any real Gulf Stream realization.

Figure 11a shows the density anomaly field at 200 m at day 14 of the evolution, which corresponds in real time to 18 May 1988. The model still retains some memory of the initial state as the warm core ring that is trapped inside the northward steepening meander is still present, and a smaller ring structure is beginning to appear in the trough of the southern meander. For comparison, we show in Fig. 11b the density anomaly field

Unauthenticated | Downloaded 06/21/21 02:08 AM UTC

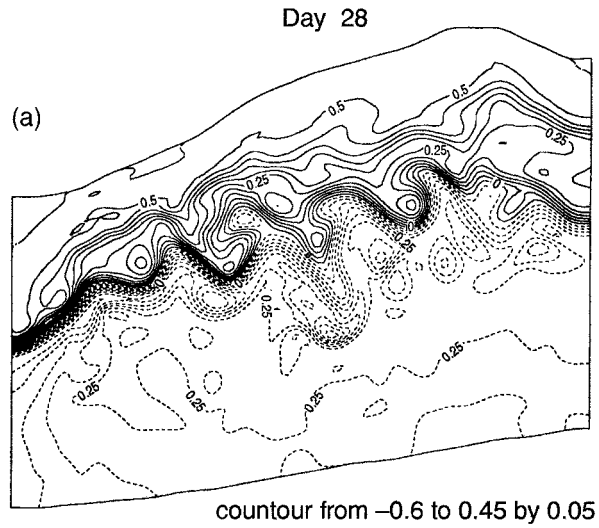

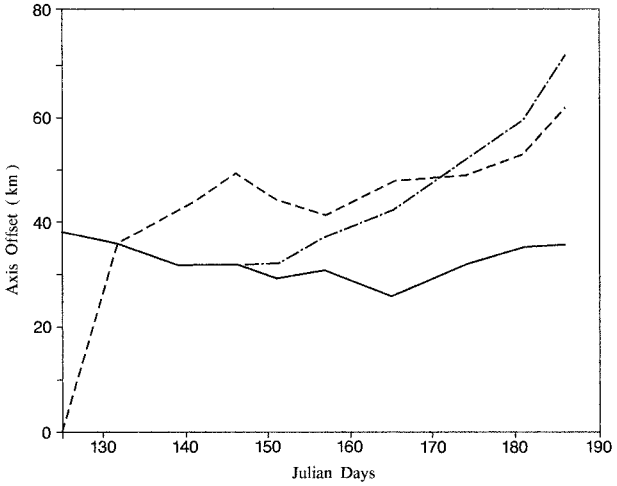

FIG. 13. North wall mean offset from IR imagery for persistence test, dashed line; 2-month assimilation of OTIS-3b, solid line; OTIS-3b assimilation interrupted at day 146 and successive unconstrained evolution, dotted–dashed line.

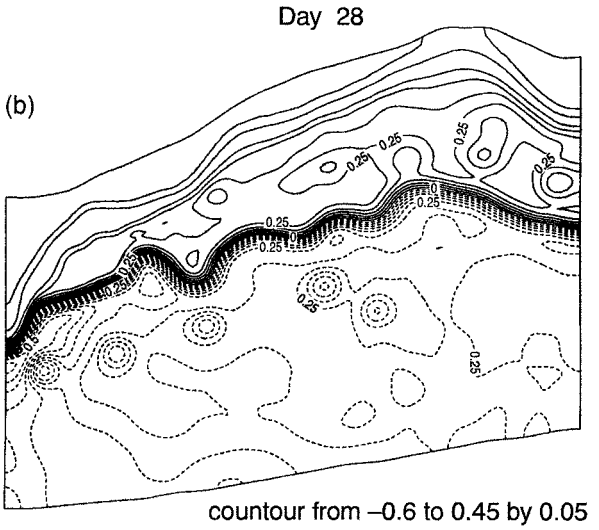

FIG. 12. (a) As in Fig. 11a but after 28 days of unconstrained evolution. (b) As in Fig. 11b but at day 28, real time 1 June 1988.

at 200 m from the corresponding OTIS-3 dataset. By day 28 of the evolution shown in Fig. 12a (real-time date of 1 June 1988), the model has completely lost the memory of its initial state. A rich series of unstable meanders is seen to be growing. The actual Gulf Stream pattern for 1 June 1988 for the OTIS-3a dataset is shown in Fig. 11b and can be seen to be completely different. The unconstrained evolution of Figs. 11a and 12a is remarkably similar to the unconstrained jet evolution obtained initializing the model with the OTIS-3a package by using the sea surface height, shown in Figs. 4a and 5a of Malanotte-Rizzoli and Young (1995). Figures 11 and 12 show qualitatively that SPEM predictability time is less than 4 weeks, on the order of 2–3 weeks, as shown quantitatively in Malanotte-Rizzoli and Young (1995).

We want to assess more quantitatively SPEM predictive skill under a better initialization than those previously discussed. Specifically, we let the model evolve unconstrained after 21 days of OTIS-3b assimilation (Table 2) during which time the initial OTIS fields are dynamically adjusted by the assimilation itself. In Fig. 13 we show the north wall mean offset from IR imagery over the 2 months of the DAMEE GSR phase III experiment for (i) persistence test (dashed line), (ii) intermittent assimilation over 2 months of the OTIS-3b dataset (solid line), and (iii) experiment in which the OTIS-3b assimilation is turned off after 21 days at Julian day 146, and the model is allowed to evolve unconstrained for the remaining 39 days (dotted–dashed line). As is clear from Fig. 13, the model predictability time is approximately 25 days, and the model significantly beating persistence is approximately 3 weeks. This result further confirms that SPEM predictive skill is in the 2–3-week range, depending on the goodness of the initial condition.

b. Intermittent assimilations at different frequencies

For effective assimilation, data need to be available at time intervals that are shorter than the timescale over which the model loses the memory of the initial state, that is, the model predictability timescale. To establish this timescale, Malanotte-Rizzoli and Young (1995) used two approaches. The first approach was based upon carrying out a traditional predictability experiment in which the prognostic variables are perturbed at the initial time by a random perturbation (Lilly 1972; Malanotte-Rizzoli 1982). The predictability timescale is then defined as the *e*-folding time of the exponential growth

Unauthenticated | Downloaded 06/21/21 02:08 AM UTC

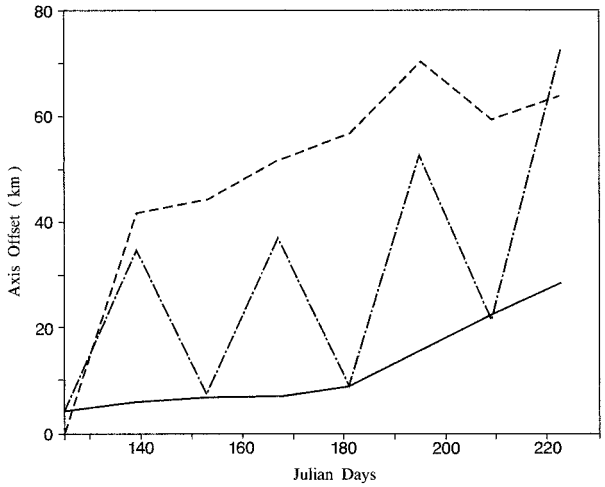

FIG. 14. Assimilation of biweekly OTIS-3a data. Dashed line: persistence compared to IR north wall; solid line: data assimilated every 14 days; dotted–dashed line: data assimilated every 28 days.

of the error between the perturbed and unperturbed fields. Such an experiment was carried out and monitored the rms error growth between the perturbed and unperturbed density fields at 200 m. By day 30, the rms error had grown to approximately three times the initial value, and by day 45 it had grown by an order of magnitude. Thus, 30 days can be taken as a measure of the predictability time for the model.

The second approach was based upon measuring the model north wall mean offset in the unconstrained evolution from the IR imagery north wall. This also gave a predictability timescale of approximately 30 days, defining it as the time over which the model beats persistence (Malanotte-Rizzoli and Young 1995). Figure 6b showing the model-to-model north wall mean offset starting from two different initializations having significantly different initial jet profiles indicates that after 1 month the two evolutions have diverged to give a mean offset twice as large as the error bar of the IR north wall estimate. We can then assume 30 days to be an upper bound of the frequency of intermittent datasets for the assimilation to be successful.

In this section we carry out two assimilations of OTIS-3 with biweekly and monthly frequency. However, the OTIS-3b data were available only for 2 months, see Table 2, which is a period too short to carry out these assimilations. Even though OTIS-3a data were not available at the dates of Table 2, we have biweekly OTIS-3a data starting on 4 May and ending on 28 December 1988 in the context of SYNOP work. Thus, we used these OTIS-3a datasets for the biweekly versus monthly assimilations. Figure 14 shows the model north wall mean offsets from IR north wall starting on 4 May 1988 for biweekly assimilation (solid line), monthly assimilation (dotted–dashed line), and persistence (dashed line). We stop the experiment at Julian day 225, 100 days into the evolution, when the monthly assimilation exceeds persistence. As evident from Fig. 14, over 100 days the biweekly assimilation performs very well, exceeding 20 km only in the very final 15 days. The monthly assimilation, on the other hand, performs much more poorly, with a maximum increase of the mean north wall offset just in the middle of the monthly assimilation cycle. At day 100, the assimilation becomes worse than persistence.

We conclude that a weekly frequency of OTIS-3 assimilation is not necessary; biweekly assimilations still ensure an excellent predictive skill of the Gulf Stream front.

5. Conclusions

In this paper we address issues related to the DAMEE GSR effort, whose main focus was to assess the forecast capability of different models when initialized with common fields and how subsequent assimilations of the global OTIS-3 dataset would impact such forecasting skill. The objective of DAMEE GSR phases I and II were short duration forecasting experiments, 1 to 2 weeks. Phase III extended the suite of case studies by adding a long duration (2 months) experiment with intermittent assimilation of OTIS-3 data, spaced at an average frequency of 1 week. We report the results of such an experiment and we insert it in a broader perspective addressing two further issues, namely, the sensitivitiy of the model to the choice of the initial field and to the frequency of data assimilation. Our main results can be summarized as follows.

First, the intermittent assimilation of the OTIS-3b datasets with an average weekly frequency has a very profound impact on the model forecasting skill. In the unconstrained evolution; that is, with no data assimilation, the model never beats persistence. With the assimilation, the model-predicted north wall is in excellent agreement with the verification IR north wall in a long duration (2 months) experiment, remaining basically always within the error bar of the IR north wall estimate, ± 15 km.

Second, two OTIS-3 datasets were available, which we call OTIS-3a and OTIS-3b, providing slightly different three-dimensional distributions of temperature and salinity, and hence density. Two types of sensitivity tests were carried out: reconstruction of initial fields with the two different datasets but the same initialization method; reconstruction of initial fields with the same dataset but different initialization methods. Unconstrained prognostic calculations were then carried out starting from these different initial conditions. The results show that the initial velocity field is much more crucial in affecting the model evolution and hence its predictive skill as it determines the stability properties of the Gulf Stream jet. An identical initialization procedure based upon assuming a level of no motion at 2000 m reconstructs Gulf Stream jets very similar in vertical and horizontal structures as well as in strength from the two

Unauthenticated | Downloaded 06/21/21 02:08 AM UTC

different OTIS-3 datasets. Consequently, the related model evolutions remain close for a long duration, about 40 days, as proved by the mean offset of the model north walls in the two experiments. On the other hand, the use of different initialization methods even with the same OTIS-3a dataset provides two rather different initial jets that evolve in a rapidly diverging manner. Hence, it is important to consistently use the same dynamical initialization for velocity when dealing with slightly different density distributions in order to compare meaningfully experiments with different initial fields.

Finally, we compare the weekly assimilations of OTIS-3b available for the DAMEE GSR phase III with biweekly and monthly assimilations of OTIS-3a available from 4 May 1988 through 23 December 1988, always using the same initialization for OTIS-3a and OTIS-3b datasets. We conclude that a weekly assimilation of the global OTIS-3 dataset is not necessary and that a biweekly assimilation is equally effective in improving the model predictive skill in a statistically significant manner over long duration assimilations.

Acknowledgments. This research was carried out with the support of the Office of Naval Research Grant N00014-90-J-1481. We thank Wen Qian for producing the OTIS-3 runs for the case study periods of the DAMEE GSR program. We thank the Harvard University Gulfcast group for providing the software giving us the framework for the Gulf Stream axis analysis algorithms used in this paper. We also thank G. R. Flierl for helping us gather the Hall and Fofonoff cruise data into a usable form through the software he developed as a part of the JGOFS data management program.

APPENDIX

The SPEM Model

The model equations of motion are those for an incompressible, hydrostatic, Boussinesq rotating fluid—the vertical coordinate is transformed from the Cartesian depth z to a topography-following σ coordinate defined as

$$\sigma = 1 + 2\left(\frac{z}{h}\right), \tag{A1a}$$

where $h(x, y)$ is the bottom relief. Thus, for

$$-h \le z \le 0$$

it follows that

$$-1 \le \sigma \le +1, \tag{A1b}$$

σ-coordinate models may produce large errors in the estimates of the pressure gradient forces (Haney 1991). The spatially dependent Shapiro smoothing algorithm (J. Wilkins 1992, personal communication) ensures that topographic slopes are everywhere moderate. The pressure gradient errors are kept minimal by subtracting the mean density profile $\overline{\rho}(z)$ from the total density before calculating the dynamic pressure p/ρ_0 (Beckmann and Haidvogel 1993). A horizontal orthogonal transformation is then carried out to coastal-following coordinates,

$$\xi(x, y) = \text{along-coast coordinate}$$
$$\eta(x, y) = \text{coastward coordinate},$$

defined by

$$(ds)_\eta = \left(\frac{1}{m}\right)d\xi$$

and

$$(ds)_\xi = \left(\frac{1}{n}\right)d\eta, \tag{A2}$$

where $m(x, y)$ and $n(x, y)$ are the scale factors relating the distances $D\xi$ and $D\eta$ to the physical arc-length Ds.

The resulting equations of motion in the (ξ, h, s) coordinate system are

$$\begin{aligned}
&\frac{\partial}{\partial t}\left(\frac{hu}{mn}\right) + \frac{\partial}{\partial \xi}\left(\frac{hu^2}{n}\right) + \frac{\partial}{\partial \eta}\left(\frac{huv}{m}\right) + \frac{\partial}{\partial \sigma}\left(\frac{hu\omega}{mn}\right) \\
&\quad - \left[\left(\frac{f}{mn}\right) + v\frac{\partial}{\partial \xi}\left(\frac{1}{n}\right) - u\frac{\partial}{\partial \eta}\left(\frac{1}{m}\right)\right]hv \\
&\quad = -\left(\frac{h}{n}\right)\frac{\partial \phi}{\partial \xi} + (1 - \sigma)\left(\frac{gh\rho}{2\rho_0 n}\right)\frac{\partial h}{\partial \xi} \\
&\qquad - \frac{1}{T_{\text{dmp}}}\left[\frac{h(u - u_{\text{ref}})}{mn}\right] + v\left(\frac{h}{mn}\right)\nabla^4 u \\
&\qquad + \frac{4}{h}\frac{\partial}{\partial \sigma}\left[\kappa\frac{\partial}{\partial \sigma}\left(\frac{u}{mn}\right)\right],
\end{aligned} \tag{A3a}$$

$$\begin{aligned}
&\frac{\partial}{\partial t}\left(\frac{hv}{mn}\right) + \frac{\partial}{\partial \xi}\left(\frac{huv}{n}\right) + \frac{\partial}{\partial \eta}\left(\frac{hv^2}{m}\right) + \frac{\partial}{\partial \sigma}\left(\frac{hv\omega}{mn}\right) \\
&\quad - \left[\left(\frac{f}{mn}\right) + v\frac{\partial}{\partial \xi}\left(\frac{1}{n}\right) - u\frac{\partial}{\partial \eta}\left(\frac{1}{m}\right)\right]hu \\
&\quad = -\left(\frac{h}{m}\right)\frac{\partial \phi}{\partial \eta} + (1 - \sigma)\left(\frac{gh\rho}{2\rho_0 m}\right)\frac{\partial h}{\partial \eta} \\
&\qquad - \frac{1}{T_{\text{dmp}}}\left[\frac{h(v - v_{\text{ref}})}{mn}\right] + v\left(\frac{h}{mn}\right)\nabla^4 v \\
&\qquad + \frac{4}{h}\frac{\partial}{\partial \sigma}\left[\kappa\frac{\partial}{\partial \sigma}\left(\frac{v}{mn}\right)\right],
\end{aligned} \tag{A3b}$$

Unauthenticated | Downloaded 06/21/21 02:08 AM UTC

$$\frac{\partial}{\partial t}\left(\frac{h\rho}{mn}\right) + \frac{\partial}{\partial \xi}\left[\frac{hu(\rho + \overline{\rho})}{n}\right] + \frac{\partial}{\partial \eta}\left[\frac{h\upsilon(\rho + \overline{\rho})}{m}\right] + \frac{\partial}{\partial \sigma}\left[\frac{h\omega(\rho + \overline{\rho})}{mn}\right] = -\frac{1}{T_{\text{dmp}}}\left[\frac{h(\rho - \rho_{\text{ref}})}{mn}\right] + \upsilon\left(\frac{h}{mn}\right)\nabla^4\rho + \frac{4}{h}\frac{\partial}{\partial \sigma}\left[\kappa\frac{\partial}{\partial \sigma}\left(\frac{\rho}{mn}\right)\right], \tag{A3c}$$

$$\phi = \phi_s - \int_{\sigma}^{0}\left(\frac{gh\rho}{2\rho_0}\right)d\sigma, \tag{A3d}$$

$$\frac{\partial}{\partial \xi}\left(\frac{hu}{n}\right) + \frac{\partial}{\partial \eta}\left(\frac{h\upsilon}{m}\right) + \frac{\partial}{\partial \sigma}\left(\frac{h\omega}{mn}\right) = 0, \tag{A3e}$$

where

(u, υ, ω)	the (ξ, η, σ) velocity components
$\rho^* = \rho_0 + \overline{\rho}(z) + \rho(x, y, z, t) = \rho_0 + \overline{\rho}(\xi, \eta, \sigma) + \rho(\xi, \eta, \sigma, t)$	the total density
$\phi(\xi, \eta, \sigma, t)$	the dynamic pressure p/ρ_0
$\phi_S(\xi, \eta, t)$	the surface pressure
$f(\xi, \eta)$	the real Coriolis parameter evaluated in a spherical coordinate system covering the model domain
g	the gravitational acceleration
ν	horizontal eddy viscosity and diffusivity
$\nabla^4 = \nabla^2\nabla^2$	the biharmonic operator

with

$$\nabla^2 = \left(\frac{mn}{h}\right)\left[\frac{\partial}{\partial \xi}\left(\frac{mh}{n}\right)\frac{\partial}{\partial \xi} + \frac{\partial}{\partial \eta}\left(\frac{nh}{m}\right)\frac{\partial}{\partial \eta}\right]$$

and the velocity σ coordinate is defined by

$$\omega(\xi, \eta, \sigma, t) = \frac{1}{h}\left[(1 - \sigma)um\frac{\partial h}{\partial \xi} + (1 - \sigma)\upsilon n\frac{\partial h}{\partial \eta} + 2w\right]. \tag{A4}$$

There is no vertical diffusion ($\kappa = 0$). Shapiro filtering of the eighth order is done on the time-evolved vorticity and density fields.

The vertical boundary conditions are specified as follows. At the surface, $\sigma = 1$:

$$\left(\frac{2\kappa}{h}\right)\frac{\partial u}{\partial \sigma} = \tau_x^0(x, y, t) = 0,$$

$$\left(\frac{2\kappa}{h}\right)\frac{\partial \upsilon}{\partial \sigma} = \tau_y^0(x, y, t) = 0,$$

$$\left(\frac{2\kappa}{h}\right)\frac{\partial \rho}{\partial \sigma} = \tau_\rho^0(x, y, t) = 0,$$

$$\omega = 0. \tag{A5}$$

At the bottom, $\sigma = -1$:

$$\left(\frac{2\kappa}{h}\right)\frac{\partial u}{\partial \sigma} = \tau_x^h(x, y, t) = 0,$$

$$\left(\frac{2\kappa}{h}\right)\frac{\partial \upsilon}{\partial \sigma} = \tau_y^h(x, y, t) = 0,$$

$$\left(\frac{2\kappa}{h}\right)\frac{\partial \rho}{\partial \sigma} = 0,$$

$$\omega = 0. \tag{A6}$$

The vertical calculations are spectral; that is, the model prognostic variables (u, υ, ρ) are expanded into a finite polynomial basis set $P_n(s)$. An example of one such expansion would be

$$\begin{pmatrix} u \\ \upsilon \\ \rho \end{pmatrix}(\xi, \eta, \sigma, t) = \sum_{n=0}^{N}\begin{vmatrix} a_n^u(\xi, \eta, t) \\ a_n^\upsilon(\xi, \eta, t) \\ a_n^\rho(\xi, \eta, t) \end{vmatrix} P_n(\sigma), \tag{A7}$$

where $P_n(s)$ are the modified Chebyshev polynomials defined by

$$P_n(\sigma) = \begin{cases} 1 & \text{for } n = 0, \\ T_n(\sigma) & \text{for } n > 0,\ n \text{ being odd}, \\ T_n(\sigma) + \dfrac{1}{n^2 - 1} & \text{for } n > 0,\ n \text{ being even}, \end{cases} \tag{A8}$$

and $T_n(s) = \cos(n \arccos s)$ is the nth order Chebyshev polynomial. The basic polynomials satisfy the constraint

$$\frac{1}{2}\int_{-1}^{1} P_n(\sigma)\, d\sigma = \delta_{0n}; \tag{A9}$$

that is, only the $n = 0$ polynomial (constant) has a nonzero vertical integral and represents the barotropic mode of the system. The $N = 13$ specially constructed numerical polynomials are used in these simulations where the $n = 0$ polynomial represents the barotropic mode. The modal amplitudes $a_n(\xi, \eta, t)$ are furthermore sampled at a number of vertical collocation points defined as the location of the extrema of the highest-order polynomial, which is 12 in our case. The use of Chebyshev polynomials as vertical basis ensures increased

Unauthenticated | Downloaded 06/21/21 02:08 AM UTC

vertical resolution at the surface and bottom boundaries. However, in a region like the Gulf Stream characterized by a very sharp permanent pycnocline, this must be adequately resolved to account properly for the internal dynamics and baroclinic instabilities of the Gulf Stream jet and associated eddy field. Thus, the polynomial dependence on the vertical coordinate σ is scaled by a prescribed mean density profile $\overline{\rho}(z)$ representative of the climatological condition of the region. The construction of the mean profile $\overline{\rho}(z)$ is discussed in the text. This vertical coordinate stretching creates a set of numerical polynomials that allows for a better vertical resolution of the fluid structure (denser number of collocation points in the region of the permanent pycnocline).

In the (ξ, η) plane a centered second-order finite-difference scheme is used, following the well-known Arakawa C grid for the arrangement of variables (Arakawa and Lamb 1977). The first moments of (u, v, ρ) are conserved, corresponding to the volume-averaged budgets of momentum and density. The N internal modes of (u, v) are obtained by time integration of the horizontal momentum equations after removing the depth-averaged component. Similarly, the mean vertical profile $\overline{\rho}(z)$ is subtracted from the total density field to avoid the production of large errors in the evaluation of the pressure gradient force, as discussed in the text. A traditional leapfrog time stepping scheme is used with trapezoidal correction every 12 time steps to remove the computational mode. With the rigid-lid approximation, the surface pressure field $\phi_s(\xi, \eta)$ remains unknown. As the depth-integrated flow is horizontally nondivergent, a transport streamfunction can be defined as

$$\overline{u} = -\left(\frac{n}{h}\right)\frac{\partial \Psi}{\partial \eta}$$

and

$$\overline{v} = \left(\frac{m}{h}\right)\frac{\partial \Psi}{\partial \xi}. \tag{A10}$$

The (unknown) surface pressure contribution is removed by taking the curl of the depth-integrated momentum equations from which a prognostic equation is obtained for the generalized barotropic vorticity:

$$\zeta^* = \nabla^2 \Psi(\zeta, \eta, t). \tag{A11}$$

This is then integrated in time according to the time stepping algorithm described above to obtain the time-varying transport streamfunction $\Psi(\xi, \eta, t)$ from which the time-evolved barotropic components of the velocities are evaluated. The horizontal boundary conditions on Ψ are evaluated from the global dataset OTIS-3, as described in section 2c of the paper.

REFERENCES

Chapman, D. C., 1985: Numerical treatment of cross-shelf open boundaries in a barotropic coastal ocean model. *J. Phys. Oceanogr.,* **15,** 1060–1075.

——, and K. H. Brink, 1987: Shelf and slope circulation induced by fluctuating offshore forcing. *J. Geophys. Res.,* **92,** 11 741–11 759.

Cornillon, P., and D. R. Watts, 1987: Satellite thermal infrared and inverted echo sounder determinations of the Gulf Stream northern edge. *J. Atmos. Oceanic Technol.,* **4,** 712–723.

Cummings, J. A., and M. Ignaszewski, 1991: The Fleet Numerical Oceanography Center regional ocean analysis system. *Proc. MTS '91 Conf.,* New Orleans, LA, Marine Technological Society, 1123–1129.

Glenn, S. M., D. Crout, and A. L. Perkins, 1991: Comparison of Gulf Stream forecast model initialization and verification analyses. Institute of Naval Oceanography Tech. Memo. TM-6, 37 pp. [Available from Stennis Space Center, Stennis Space Center, MS 39529.]

Haidvogel, D. B., J. Wilkins, and R. E. Young, 1991: A semi-spectral primitive equation coastal ocean circulation model using vertical sigma and horizontal curvilinear coordinates. *J. Comput. Phys.,* **94,** 151–185.

Halkin, D., and T. Rossby, 1985: The structure and transport of the Gulf Stream at 73°W. *J. Phys. Oceanogr.,* **15,** 1439–1452.

Hall, M. M., and N. P. Fofonoff, 1993: Downstream development of the Gulf Stream from 68°W to 55°W. *J. Phys. Oceanogr.,* **23,** 225–249.

Lai, C. A., and W. Qian, 1993: Preparation of data assimilation and model evaluation experiment datasets. Center for Ocean and Atmospheric Modeling Tech. Rep., TR 1-94, Stennis Space Center, MS, 127 pp. [Available from Stennis Space Center, MS 39529.]

Lilly, D. K., 1972: Numerical simulation studies of two-dimensional turbulence. II. Stability and predictability studies. *Geophys. Fluid Dyn.,* **4,** 1–28.

Malanotte-Rizzoli, P., 1982: The predictability problem of planetary motions. *Topics in Ocean Physics,* A. R. Osborne and P. Malanotte-Rizzoli, Eds., North-Holland Publishing, 184–204.

——, and R. E. Young, 1995: Assimilation of global versus local data sets into a regional model of the Gulf Stream system. Part I: Data effectiveness. *J. Geophys. Res.,* **100,** 24 773–24 796.

Semtner, A. J., 1974: An ocean general circulation model with bottom topography, Numerical simulation of weather and climate. Dept. of Meteorology UCAR, Tech. Rep. 9, 99 pp.

UNESCO, 1981: Tenth report of the joint panel on oceanographic tables and standards. UNESCO Tech. Papers in Marine Science 36, UNESCO, Paris, France, 25 pp.

Willems, R. C., and Coauthors, 1994: Experiments evaluate ocean models and data assimilation in the Gulf Stream. *Eos, Trans. Amer. Geophys. Union,* **75** (34), 385–394.

Unauthenticated | Downloaded 06/21/21 02:08 AM UTC